Ultrahigh active material content and highly stable Ni-rich cathode leveraged by oxidative chemical vapor deposition

Yuxuan Zhang¹, Chung Soo Kim², Han Wook Song³, Sung-Jin Chang⁴, Hyeonghun Kim¹, Jeongmin Park², Shan Hu⁵, Kejie Zhao⁵, Sunghwan Lee¹*

¹School of Engineering Technology, Purdue University, West Lafayette, IN 47907, USA

²Analysis Technical Center, Korea Institute of Ceramic Engineering and Technology, Jinju, Gyeongsangnam-do, Republic of Korea

³Center for Mass and Related Quantities, Korea Research Institute of Standard and Science, Daejeon 34113, Republic of Korea

⁴Measurement & Analysis Team, National Nanofab Center, Daejeon, 34141, Republic of Korea ⁵School of Mechanical Engineering, Purdue University, West Lafayette, IN 47907, USA

* Corresponding authors: sunghlee@purdue.edu

Acknowledgments

Funding: This work was partially supported by the U.S. National Science Foundation (NSF) Award No. ECCS-1931088. S.L. and H.W.S. acknowledge the support from the Improvement of Measurement Standards and Technology for Mechanical Metrology (Grant No. 20011028) by KRISS.

Competing Interests

The authors declare that they have no competing interests.

Author Contributions

S.L. and Y.Z. conceived the study. Y.Z. prepared the materials, assembled cells and conducted electrochemnical evaluations. C.S.K and J.P. prepared FIB/TEM specimens and obatained TEM images. H.W.S and S.C. conducted TOF-SIMS characterizations and analysis. S.H. and K.Z. obtained SEM images of Li metal anodes. H.K. performed conductivity measurements. All authors contirubted to writing and revising manuscript.

Data and materials availability

All data needed to evaluate the conclusions in the paper are present in the paper and/or the Supplementary Materials.

Ultrahigh active material content and highly stable Ni-rich cathode leveraged by oxidative chemical vapor deposition

Keywords: Ni-rich; cathode modification; high active material ratio; primary particle coating; oCVD; PEDOT

Abstract

Despite the huge achievements that have been made in developing lithium-ion batteries, there remain gaps between the existing demands and the current battery performance. As one of the key components, cathode needs to adopt a further enhanced design to realize a high energy density and long useful life battery. Here we report a cathode tailoring strategy, exploiting multi-functional conformal coatings that are mechanically flexible, thickness controllable at the nanometer scale, electronically conductive, and selectively permeable. We demonstrate a gas phase polymerization technique that successfully enhances the energy density and the lifespan of the battery, particularly for a Ni-rich cathode (LiNi_{0.8}Co_{0.1}Mn_{0.1}O₂, NCM811). Oxidative chemical vapor deposition (oCVD) yielded an extremely conformal polymer layer of poly (3,4-ethylene dioxythiophene) (PEDOT) that is chemisorbed on both primary and secondary particles in NCM811 with identified S-O bonds. The chemo-physical adhesion between the cathode particles and highly conductive nature of oCVD PEDOT permit a significant reduction of inactive materials inclusion in the cathode and enable a noticeable high active materials content (up to 99% in weight percentage). ToF-SIMS results identified that the formation of cathode electrolyte interphases, especially between primary particles, has been eliminated in the PEDOT coated sample. As a result, the cathode enabled by multi-functional oCVD PEDOT exhibited much higher capacity retention (about 80% after 300 cycles) compared with the pristine sample (about 6% only after 200 cycles). These results offer a single-step rational cathode design strategy that ensures high-energy density, long-life, and safe lithium-ion batteries.

Introduction

The successful commercialization of lithium-ion batteries (LIBs) has led to wide utilization in customer electronic devices because of their excellent cycle performance and moderate rate capability [1, 2]. With the explosive growth of market demands for portable electronic devices such as cellphones, laptop computers, hybrid electric vehicles (HEVs), and electric vehicles (EVs), it is urged to exploit LIBs with enhanced energy density and cycle life [3, 4].

As a key component in batteries, the cathode needs to be properly engineered for the development of highenergy and long-life batteries [5-7]. The active materials in the cathode often suffer from degradation during the charge and discharge process, which generates safety issues during circulation. In addition, high concentrations of inactive materials in the cathode (conductive additives and polymer binders, up to 10%) may limit the energy density of the battery [8-10].

Considerable efforts have been made on the optimization of cathode active materials to enhance the stability and compatibility with electrolytes [11, 12]. Doping, utilizing elements including Mg, Al, and Ti, was adopted as an effective way to enhance the bulk stability and cycle life of the cathode structure [13-15]. However, several issues were also reported that these doping approaches decrease the specific capacity and lithium-ion conductivity of the cathode [13, 16]. Modifying cathode structure has also been considered to optimize the electrochemical properties and thermal stability [3]. However, the small size of the cathode active material particles led to a low tap density of the cathode and then reduced the energy density of batteries [17, 18]. It was also reported well-designed structures were destroyed during the charge and discharge process (e.g.: a modified shell exfoliated from the core) [19, 20]. Cathode coating is a widely used approach due to its ability to enhance stability and be compatible with other cathode modifications [21-23]. Zheng et al. additionally doped Zr into the La₂Zr₂O₇ coating to improve the electrochemical stability of both surface and bulk of the cathode active materials [24]. There was another effort to coat the oxide layer of Li_{1.8}Sc_{0.8}Ti_{1.2}(PO₄)₃ on the precursor of NCM 811, followed by calcination of the structure to produce the cathode, by which higher electrochemical stability was achieved [25]. However, the majority of the reported coating methods (e.g., solid-state coating matter) have been unable to achieve high conformal coverage (on both primary and secondary particles) due to the limited penetration ability of the solid-state coating materials [21, 26]. In addition, inert inorganic compounds such as metal oxides (Al₂O₃ [27], ZrO₂ [28], V₂O₅ [29]), phosphates (AlPO₄ [30], Co₃(PO₄)₂ [31]), and fluorides (AlF₃ [32]) have been reported as well and yet these coatings were delaminated from the cathode particles due to the anisotropic volume change during lithiation and delithiation [33, 34].

Inactive materials typically make up more than 10 wt% of the cathode, of which the high amount is unfavorable to achieve high energy densities. Although there have been efforts to reduce the inactive material portion in the cathode for increasing the energy density, reducing carbon concentration generally has resulted in low electronic conductivity and undesirable polarization of the cathode material with increased resistance [35, 36]. Decreasing the binder amount in the cathode has been also limited due to the loss of active materials [35, 37].

Strategically, the effective cathode coating requires (i) high conformality to protect active materials all-sided, (ii) strong chemo-physical bonding with the cathode material to prevent detachment from the active materials, (iii) mechanical flexibility to accommodate the volume change inevitably caused during the charge/discharge processes, and (iv) capability to replace (or reduce) conductive additives and polymer

binders to mitigate the issues mentioned above for the cathode.

The oCVD technique is an emerging deposition process that generates conjugated polymer films via a gas phase reaction with greater conductivity as well as superior uniformity and conformality compared to conventional solution-processed counterparts [38, 39]. In the previous report by Xu et al. [24], the oCVD technique was employed to coat a uniform poly (3,4-ethylene dioxythiophene) PEDOT layer on cathode powders (LiNi_{1/3}Co_{1/3}Mn_{1/3}O₂, NCM111) and reported enhanced electrochemical stability of the cathode material during battery cycling. The vapor-phased coating process has been verified to realize the infiltration of coating substances into the gaps between the primary particles. To further extend the application of high-electronic conductivity and adhesive functionality through the oCVD technique, our present study is uniquely contributed to new technological advancements in: (1) effectively reducing the content of the conductive additives down to 1% by utilizing the high electronic conductivity of oCVD PEDOT to generate a highly efficient electronic network; (2) completely eliminating traditional polymer binder (i.e., polyvinylidene fluoride) in the cathode by providing the intrinsic adhesive ability through conformally coated oCVD PEDOT between cathode particles; (3) visually quantifying the composition and thickness information of the cathode electrolyte interphases (CEIs) via time-of-flight secondary ion mass spectrometry (TOF-SIMS) to reveal the protection mechanism of the oCVD PEDOT for the cathode active materials for the first time; (4) achieving highly stable battery performance with Ni-rich cathode materials of LiNi_{0.8}Co_{0.1}Mn_{0.1}O₂ (NCM811), which is selected as a model system to objectively evaluate our strategies and hypothesis for NCM811 cathode modification. To the best of our knowledge, this is the first time demonstration that the oCVD technique is adopted as the electrode manufacturing process to increase the energy density and the electrochemical performance of the battery, particularly with Ni-rich cathode, NCM811 rather than NCM111 or other low Ni cathode, as schematically demonstrated in Fig. 1. By utilizing the oCVD method, a PEDOT layer can be conformally deposited on the surface of NCM811 particles, the weight ratio of active materials unprecedentedly reaches 99 wt% in the cathode. The optimized cathode showed 196 mAh g⁻¹ at 1C and 90% and 80% capacity retention after 200 and 300 cycles under 1C (1C = 200 mA g⁻¹), respectively. However, the counterpart battery (same composition without oCVD PEDOT coating) showed only 6% capacity after only 200 cycles. Additionally, time-of-flight secondary ion mass spectrometry (TOF-SIMS) reveals, for the first time, oCVD PEDOT effectively restricts the formation of cathode electrolyte interphase (CEI) on the secondary particle and eliminates the CEI between primary particles. Characterizations of the lithium metal anode paired with oCVD PEDOT after different circulation numbers demonstrate dense morphology and notable electrochemical properties, compared to that without oCVD PEDOT. The multi-functional cathode coat strategy demonstrates significant promises of achieving a high weight ratio of active materials (99 wt%) and suggests a pathway leading to the realization of higher energy density batteries.\

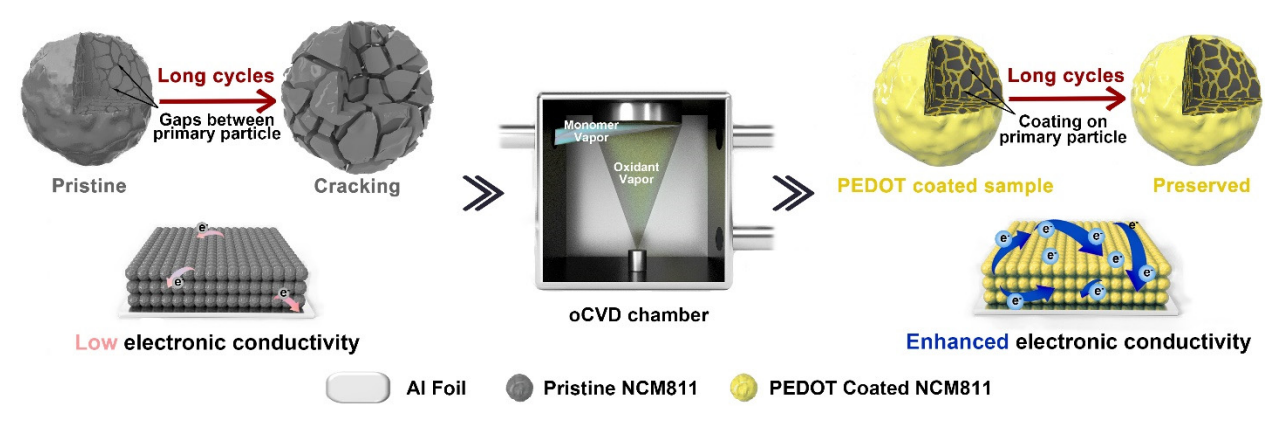


Fig. 1 Schematic of vapor-phase synthetic process of Ni-rich cathode modified with highly conformal oCVD PEDOT

Results and Discussion

Characterization of cathode materials

Through XRD and Rietveld refinement analysis shown in Fig. S1, the degree of Ni/Li cation mixing was determined for both pristine and PEDOT-55, which is found to be 4.28 and 4.37% (Table S1), respectively, indicating the oCVD PEDOT coating sustains the intrinsic crystalline structure of the pristine cathode with no significant crystallographic distortion. The nearly identical cation mixing ratio is likely attributed to the low-temperature process with the oCVD technique. Fourier-transform infrared spectroscopy (FTIR) was used to compare the chemical bonding information of oCVD PEDOT-coated NCM811 to that of a control oCVD PEDOT sample on a Si substrate. In Fig. 2a, the FTIR peaks of the NCM811 coated with 55 nmthick PEDOT (PEDOT-55) concur well with those of the control PEDOT, exhibiting a peak at ~1500-1600 cm⁻¹ due to C=C stretching in the thiophene ring and other typical peaks found in PEDOT including peaks at ~1500-1350 cm⁻¹ due to C-C stretching and C-H bending. The similar FTIR spectra between PEDOT-55 and bare PEDOT samples confirm successful oCVD PEDOT coating on NCM811 while maintaining typical PEDOT chemical bonding. The surface morphology of pristine NCM811 and oCVD PEDOT coated NCM811 was investigated using scanning electron microscopy (SEM). In Fig. 2b, an SEM image of pristine NCM811 particles shows a typical polycrystalline microstructure with spherical secondary particles, consisting of fine-grained primary particles. These microstructures are well maintained in PEDOT coated NCM811 (Fig. 2c), in which a continuous and uniform coating layer is visible on the surface.

To confirm that the oCVD PEDOT layer has been conformally coated on both primary and secondary particles, samples with about 55 nm thick oCVD PEDOT were prepared for TEM observations. The well-ordered lattice fringes are observed in Fig. S3 indicated the NCM811 particle of the PEDOT-55 specimen is highly crystallized. The corresponding Fast Fourier Transform (FFT) pattern of the selected square in Fig. S3a confirms the layered structure of PEDOT-55 (oCVD PEDOT-coated NCM) from Fig. S3b, which is well paralleled with XRD results. As clearly demonstrated in Fig. 2d and e, the oCVD PEDOT layer homogeneously covers the secondary particle. The oCVD PEDOT coat is identified by the yellow lines in Fig. 2d. Furthermore, the micro-voids between primary particles have been filled with the oCVD PEDOT (marked by the yellow arrows in Fig. 2e). The oCVD technique has successfully realized the conformal and thin PEDOT layer on and between primary particles. From energy-dispersive X-ray spectrometry (EDS)

elemental mapping in Fig. 2f, a randomly selected area (marked by red rectangular in Fig. 2f) evidently reveals that the presence of S (indicative of PEDOT) is more concentrated in the micro gaps between the primary particles, confirming the successful formation of PEDOT on the primary particles. The elements of Ni, Co, and Mn of NCM particles are found to be well distributed in the range of primary particles. To further investigate the chemical environments and valence states of major elements on the surface of pristine NCM811 (upper spectra) and at the oCVD PEDOT/NCM811 interface (lower spectra), X-ray photoelectron spectroscopy (XPS) measurements were performed. Fig. 2g-i show core-level high resolution (HR) XPS spectra of major elements of S 2p, O 1s, and Ni 2p. Note that a thin layer of oCVD PEDOT (~5 nm) was used for the XPS investigations to ensure that the surface-sensitive x-ray (typically uppermost 10-20 nm) reached well in the PEDOT/NCM811 interface. The successful coating of oCVD PEDOT on NCM811 is verified by the detected characteristic XPS peaks in Fig. 2g (lower) of S 2p spin-orbit splits, S 2p1/2 (164.5 eV) and S 2p3/2 (163.6 eV) which is similar to those from pure oCVD PEDOT (see Fig. S4). The peak at binding energy (BE) around 168.8 eV is attributed to S-O bonding [40, 41], which only exists in PEDOT-enfolded NCM811. The excellent conformality and gas-phase processing of oCVD PEDOT enable the entire surface coating on NCM811 and form sturdy S-O chemical bonds. No S information is detected in the upper XPS spectrum of the pristine cathode. Fig. 2h shows HR O 1s XPS spectra of PEDOTenfolded NCM811. Both O 1s XPS spectra can be deconvoluted to two peaks, one (weak, red) at a lower BE 529.4 eV and the other (strong, blue) at a higher BE of 531.6 eV (pristine) and 530.5 eV (PEDOT/NCM). The peak at lower BE (weak) is originated from lattice oxygen in transition metal oxides (TM-O) such as Ni-O and Mn-O [42, 43], while the peak at higher BE (strong) is attributed to non-transition metal-oxygen bonding (NonTM-O) including S-O bonding. The BE shift of NonTM-O bonding observed in the PEDOT/NCM811 specimen (530.5 eV vs 531.6 eV of pristine) is likely ascribed to the S-O bonding at the PEDOT/NCM interface, as evidenced in Fig. 2h. No shift is visible in the peak due to TM-O (BE 529.4 eV), which suggests that the lattice oxygens are preserved in the transition metal oxides without significant changes. The generation of a large amount of S-O bonding (NonTM-O bond) at the PEDOT/NCM811 interface is further enhanced from an increase in the area ratio of NonTM-O to TM-O from about 8:1 to 11:1. Fig. 2i shows a typical Ni 2p XPS spectrum of NCM811 [43, 44] presenting spin-orbit doublets of Ni 2p_{1/2} and Ni 2p_{3/2}. It should be noted that the Ni 2p peak locations remain the same in the PEDOT-enfolding sample, as displayed in Fig. 2i, which indicates that Ni in NCM811 is not involved in any chemical bonding or surface reactions during oCVD PEDOT polymerization on NCM811. The suppressed Ni 2p signals observed in Fig. 2i are simply due to the presence of the PEDOT layer on top of NCM811 particles, which reduces the x-ray penetrating distance in the NCM811. Density functional theory (DFT) calculations were further applied to investigate the cathode-PEDOT interactions. The repeating unit of PEDOT was considered to reduce the computational cost. Fig. S5a-c shows the structures of (A) a single EDOT monomer, (B) a pure LiNiO2 cathode, and (C) chemically bonded cathode-EDOT with a different angle. Each constructed structure has the minimum global Gibbs free energy as the binding energy of the system. The binding energy between EDOT and cathode surface is obtained from Eq. 1:

$$\Delta E_{binding} = \Delta E_{Cathode-EDOT} - \Delta E_{Cathode} - \Delta E_{EDOT}$$
 (1)

where $\Delta E_{binding}$ is the binding energy between LiNiO₂ and a monomer; $E_{Cathode-EDOT}$ is the total electronic energy of the optimized cathode surface and adsorbate, $E_{Cathode}$ and E_{EDOT} are the total energy of the cathode surface and EDOT when separated. Table S2 exhibits the binding energies of all structures. A portion, 42.2%

of the Cathode-EDOT binding energy is due to the electronic interactions between the cathode and EDOT (-0.89 eV out of -2.11 eV). The results further demonstrate that the oCVD PEDOT layer is chemically bonded with O on the surface of NCM811 through S-O bonds in addition to physical absorption, which supports the XPS results shown in Fig. 2g. The schematic structure of PEDOT coated NCM811 at the interface is shown in Fig. 2j.

To verify the binder property of oCVD PEDOT in our work, a movie (Supporting Movie 1) was recorded to visually compare the binder property of oCVD PEDOT-coated cathode with that of the pristine cathode. Snapshot images in Fig. S7a-c illustrate a scraping process performed on a pristine cathode sample (red rectangle) on an Al foil where the pristine active materials in this region were easily scraped from the Al foil by a swab. Fig. S7d-f shows the same scraping process made on a PEDOT-55 cathode sample (blue rectangle) where no visible differences are observed. Unlike the pristine sample that was readily scraped, the active materials in a blue box (i.e., PEDOT-55) were not scraped off, which indicates the reliable adhesive ability of oCVD PEDOT to active materials particles.

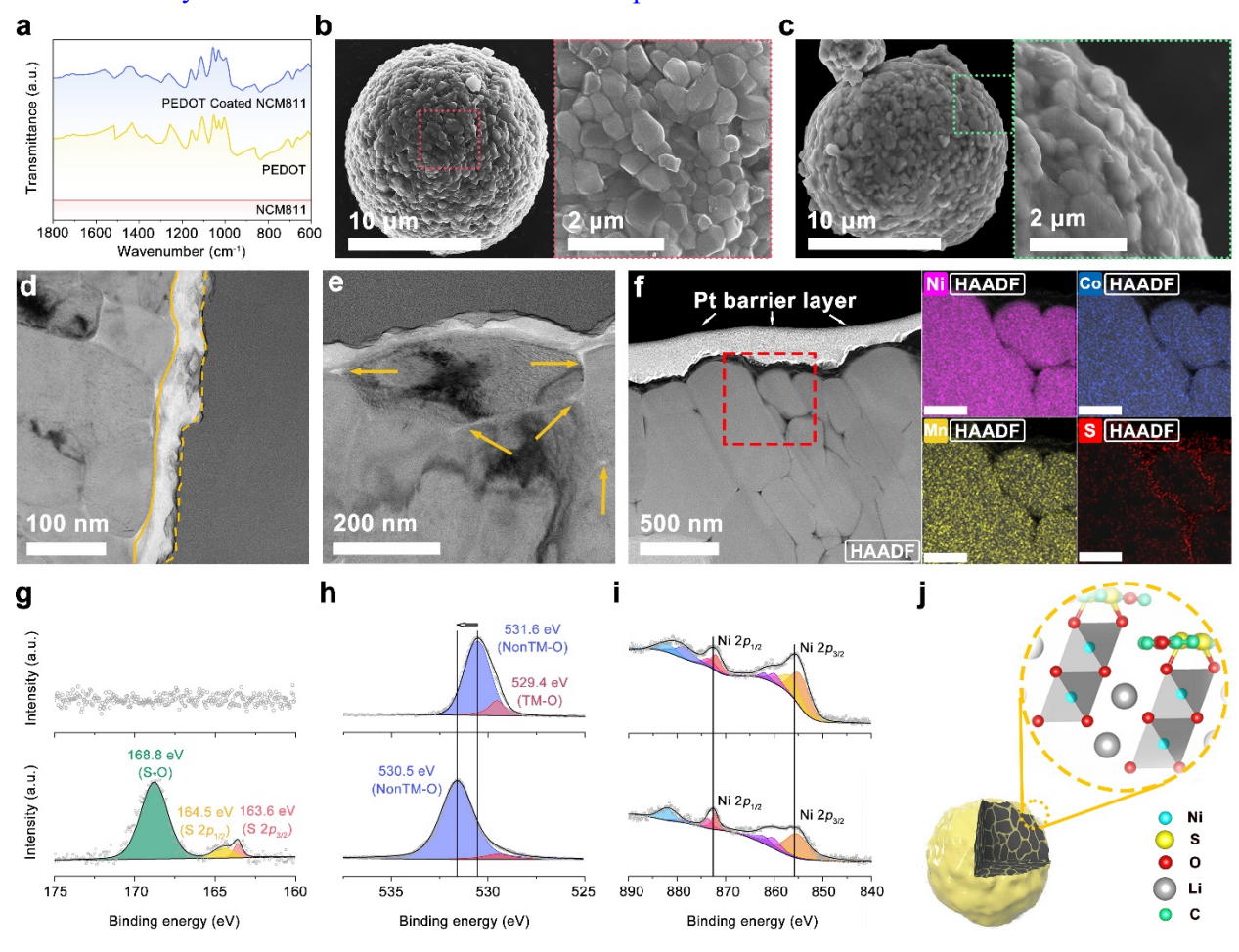


Fig. 2 Characterization of oCVD PEDOT coating. (a) Fourier-transform infrared spectra of PEDOT-55, pristine NCM811, and PEDOT. SEM images of pristine NCM811 (b) and PEDOT-55 (c). TEM images of cross-sectioned PEDOT-55 near the surface (d and e) and EDS mapping (f) of the region marked in F. Scale bars, 100 nm (EDS mapping in f). XPS spectra of S 2p (g), O 1s (h) and Ni 2p (i) for pristine NCM811 (top) and PEDOT-55 (bottom). (j) Schematic of interface structure of PEDOT-55.

Electrochemical performance investigation

To demonstrate the elevated electrochemical performance, pristine NCM811 and modified NCM811 with different thicknesses were assembled as the cathode of LIBs in coin-type half cells. When first charged/discharged at 0.1C (1C=200 mAg⁻¹) between 2.8 and 4.3V versus Li/Li⁺ at room temperature, pristine NCM811 and PEDOT-enfolded NCM811 show similar charge-discharge curves (Fig. S8), with an approximate discharge capacity and Coulombic efficiency about 207 mAh g⁻¹ and 87.6% respectively. This similar performance confirms that the PEDOT layer does not degrade the specific capacity and the chargedischarge voltage profile of NCM 811, which can be ascribed to the high electronic conductivity [45] and ionic penetrability [26] of PEDOT. The following electrochemical tests show that the cycling stability has been considerably improved by the oCVD PEDOT layer. Fig. 3a displays that the capacity retention of the oCVD PEDOT-coated cathode at 0.1C over 100 cycles was significantly enhanced to 95.3%, 97.1%, 88.2%, and 84.1% with film thicknesses of 40 nm (PEDOT-40), 55 nm (PEDOT-55), 70 nm (PEDOT-70) and 100 nm (PEDOT-100), compared to 80.5% of the pristine NCM811. Rate performance tests shown in Fig. 3b illustrate the higher specific capacity and reversibility of PEDOT-enfolded NCM811 than that of the pristine NCM811 counterpart. It should be noted that the average specific capacity achieved from PEDOT-enfolded NCM811 is significantly improved, 170.4 mAh g⁻¹ at 7C, which is 36% higher than 125.3 mAh g⁻¹ of pristine NCM811. From the capacity retention of 0.1C and rate capability under different current densities, the 55 nm film thickness is considered as an optimal oCVD condition for the best performance. As thus, the following electrochemical tests were made on PEDOT-55 and pristine NCM811. Then, a four-point probe was used to evaluate the electronic conductivity of the pristine NCM811 specimen and PEDOT-55. The conductivity of PEDOT-55 was measured to be 648 S cm⁻¹ (Fig. S9), which is more than 8 times higher than that of the pristine NCM811 sample (77 S cm⁻¹). To identify the dominant factors leading to the improved electrochemical performance in half-cells, Cyclic voltammetry (CV) measurements were carried out for both PEDOT-55 and pristine NCM811. Fig. 3c shows the initial two cycles of CV curves for both cathodes between 2.8 and 4.3 V at a sweep rate of 0.1 mV s⁻¹. The anodic and cathodic peaks for the two samples appear at similar positions in the first cycle of CV profiles, which means the lithium-ion de-/intercalation in pristine NCM811 and PEDOT-55 is located at the same potential. In the second cycle, the redox peak of PEDOT-55 is measured at 3.76 V while that of pristine is at 3.68 V. The peak potential difference ΔE ($\Delta E = E_{oxidation} - E_{reduction}$) between PEDOT-55 and pristing NCM811 is 0.09 V and 0.16 V respectively, which indicates a reduced polarization (approximately half) of the charging and discharging processes of the PEDOT-55 cathode. To further quantify the origins of the performance enhancement offered by oCVD PEDOT, coin-type half cells integrating PEDOT-55 and pristine cathode were assembled and cycled with a 1C charging and discharging rate at room temperature (Fig. 3d). Although the specific capacity of pristine NCM811 was rapidly degraded within 200 cycles (<10%), the half-cell with PEDOT-55 demonstrated greater cyclic stability during more than 300 cycles with a capacity retention of 79.1%. To solely examine the role of oCVD PEDOT deposited on NCM811, all other variables should be controlled, particularly the degradation effect of lithium anode on the battery performance, for which the anode was replaced after the 300th circulation. The specific capacity immediately increased to 173.8 mAh g⁻¹ at the 301st circulation, which illustrates there is about an 18.3 mAh g⁻¹ capacity drop caused by anode failure. Fig. 3e compares the average charging-discharging voltages between the pristine and PEDOT-modified

samples as a function of cycle. In the pristine NCM811, the voltage difference between charge and discharge increases from 0.11 (1st cycle) to 0.29 V (200th cycles), indicative of an obvious increase in polarization and impedance during cycling. In contrast, the voltage difference of PEDOT-55 slightly increased from 0.11 to 0.15 V (200th cycles), and to 0.21 V (300th cycles). In addition, the voltage difference further dropped to 0.16 V after the anode was replaced (i.e., without the effect of anode decay). Notice should also be taken in that the voltage decay was remarkably mitigated in the case of PEDOT-55 as compared to that of the pristine NCM811 shown in Fig. 3f and g. Impressively, the lithium-ion battery based on the PEDOTmodified cathode achieved an active material content up to 99%, which is significantly higher than those (mostly less than 90%) reported previously (Fig. 3h). Besides, the capacity fading per cycle for the battery modified with oCVD PEDOT is extremely small compared with those found in the literature with a similar active materials content. Detailed comparisons are summarized in Table S3. Electrochemical Impedance Spectroscopy (EIS) measurements were conducted on pristine NCM811 and PEDOT-55 batteries to investigate impedance and its variation during circulation (Fig. S10 in Supplementary Materials). In Fig. S10a (before circulation), the diameter of the semicircle of pristine NCM811 is almost twice as big as that of PEDOT-55, implying that pristine NCM811 have a larger resistance than PEDOT-55 in its initial state (103.7 versus 65.3 Ω cm²), which confirms the higher electronic conductivity of oCVD PEDOT [35, 46]. Fig. S10b illustrates the impedance spectra of half coin-type cells with pristine NCM811 and PEDOT-55 cathode materials, measured after 200 and 300 cycles, respectively. After 200 cycles, the charge transfer resistance (R_{cl}) of pristine NCM811 increased from 103.7 to 978.4 Ω cm². While for PEDOT-55 NCM811, the R_{ct} only increased from 65.3 to 259.1 Ω cm², which is approximately 75% lower than that of the pristine cell. The resistance evolution behavior of the samples clearly demonstrates the much-enhanced electrochemical performance of PEDOT-modified NCM811, and agrees well with the long cycling results shown in Fig. 3d. In addition, the ambient air storage ability was evaluated. The pristine sample and PEDOT-55 were stored in the same condition for 20 days and then were assembled in coin-type cells. In Fig. S11, after air exposure, the initial discharge capacity for the pristine NCM811 sample and PEDOT-55 decreased from 207 mAh g⁻¹ both to 182 mAh g⁻¹ and 191 mAh g⁻¹, respectively. The capacity of the pristine sample drops drastically after 10 cycles and the coulombic efficiency is only about 88% during the circulation. However, the PEDOT-55 shows much higher capacity retention after 120 cycles (73%) than that of the pristine sample (22%). It should be further noticed that the coulombic efficiency for PEDOT-55 is nearly 100%. This demonstrates an excellent ability of oCVD PEDOT to preserve the electrochemical properties of NCM811 after air exposures, which may mitigate a critical issue of cathode material storage with the limited generation of lithium compounds and NiO in ambient air conditions [47].

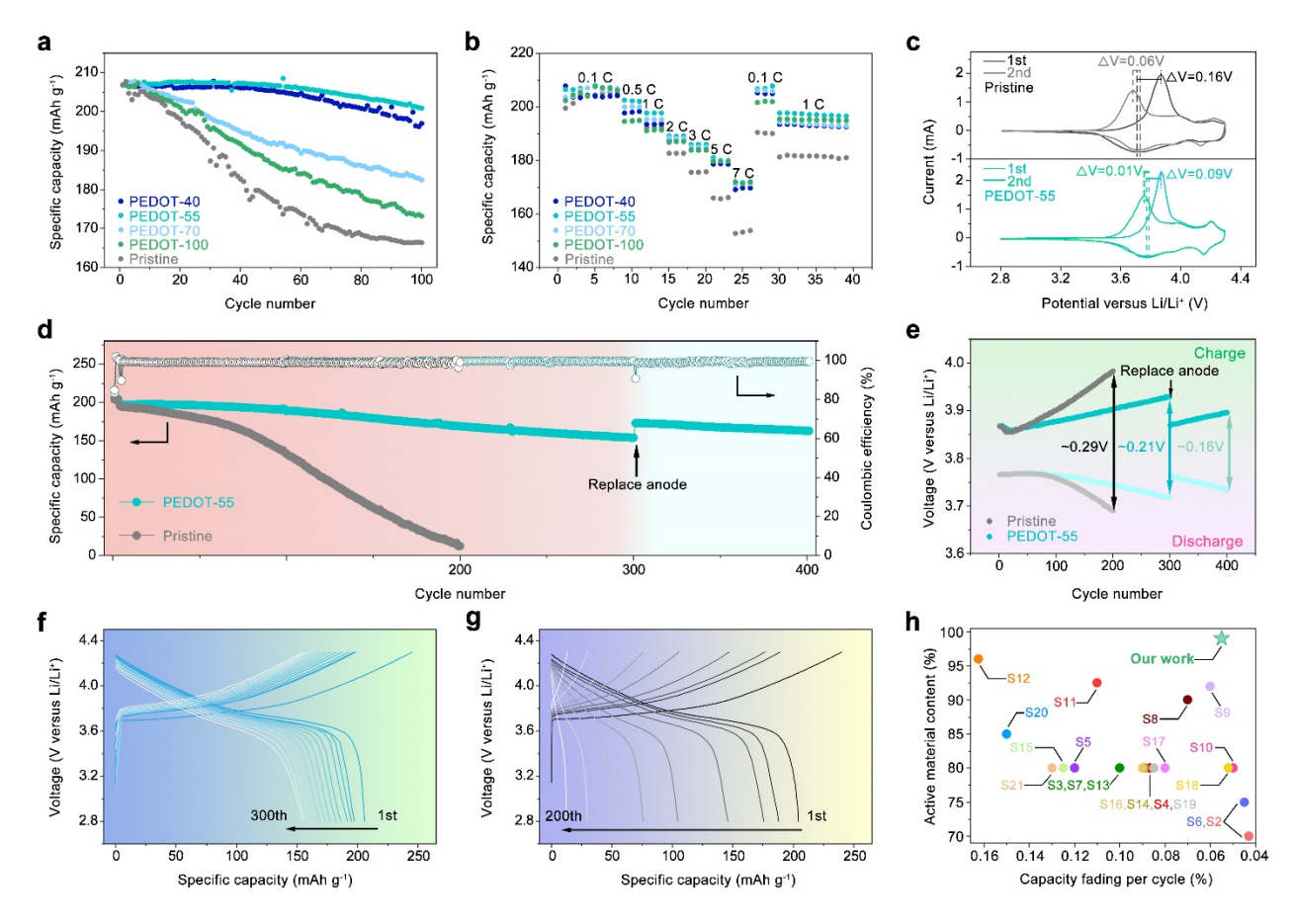


Fig. 3 Outstanding electrochemical performance of PEDOT-55 over pristine NCM. (a) Pristine and PEDOT-enfolded NCM811 capacity retention at C/10. (b) Rate capability evaluation of pristine and PEDOT-enfolded NCM811. CV curves (c) and long cycle performance and coulombic efficiency (d) of pristine NMC811 and PEDOT-55. Evolution of the average charge/discharge voltage (calculated by energy/capacity) (e) and charge-discharge profiles for pristine (f) and PEDOT-55 (g) over cycling at 1C. (h) Comparison of the electrochemical performance of lithium-ion batteries based on NCM811 cathode in our study and previous reports.

Conductivity evaluation during circulation

Galvanostatic intermittent titration technique (GITT) measurements were carried out to further investigate the electrochemical behaviors of PEDOT-55 and pristine NCM811 [48]. The batteries with both cathodes were charged and discharged in the range of 2.8-4.3 V (versus Li^+/Li) at a current density of 0.05 A g^{-1} for 30 mins, followed by an open circuit relaxation for 1 h. The diffusion coefficients of lithium ions (D_{Li^+}) are calculated using Eq. (2):

$$D_{Li^+} = \frac{4}{\pi\tau} \left(\frac{m V_m}{M S}\right)^2 \left(\frac{\Delta E_s}{\Delta E_\tau}\right)^2 \qquad (2)$$

where τ is the current pulse time, m and M are the mass of NCM811 and molecular weight, respectively. V_m is the molar volume and S is the interface between the active material and electrolyte, ΔE_s and ΔE_τ are the difference in the steady-state voltage and the total voltage difference during the galvanostatic stage [49].

In Fig. 4a and 4b of the initial charge and discharge states, the Li⁺ diffusion of the PEDOT-55 battery is close to that of the pristine NCM811 sample, which means the oCVD PEDOT coating does not hinder the transmission of lithium ions. It should be noticed that the diffusion coefficients of the pristine sample are prominently degraded for both charge and discharge processes with cycles, of which the limited diffusion of Li⁺ results from the decomposition products, blocking the Li⁺ transport at the cathode/electrolyte interface. However, the coefficients of the PEDOT-55 battery remain nearly the same with increasing the number of cycles for both charge and discharge, confirming no noticeable degradation in the Li-ion transport. These diffusion coefficient results confirm the excellent protectability of oCVD PEDOT conformally coated on the cathode. In addition, the relaxation periods of the pristine NCM811 battery after 200 cycles were less than that of the PEDOT-55 battery. The fewer relaxation periods suggest that the polarization of the pristine sample is significantly developed during circulation, which aligns well with the EIS results shown in Fig. S10. The GITT investigations further support that the functional oCVD PEDOT coating enhances the electrochemical stability of NCM811 and restricts the decomposition of the electrolyte.

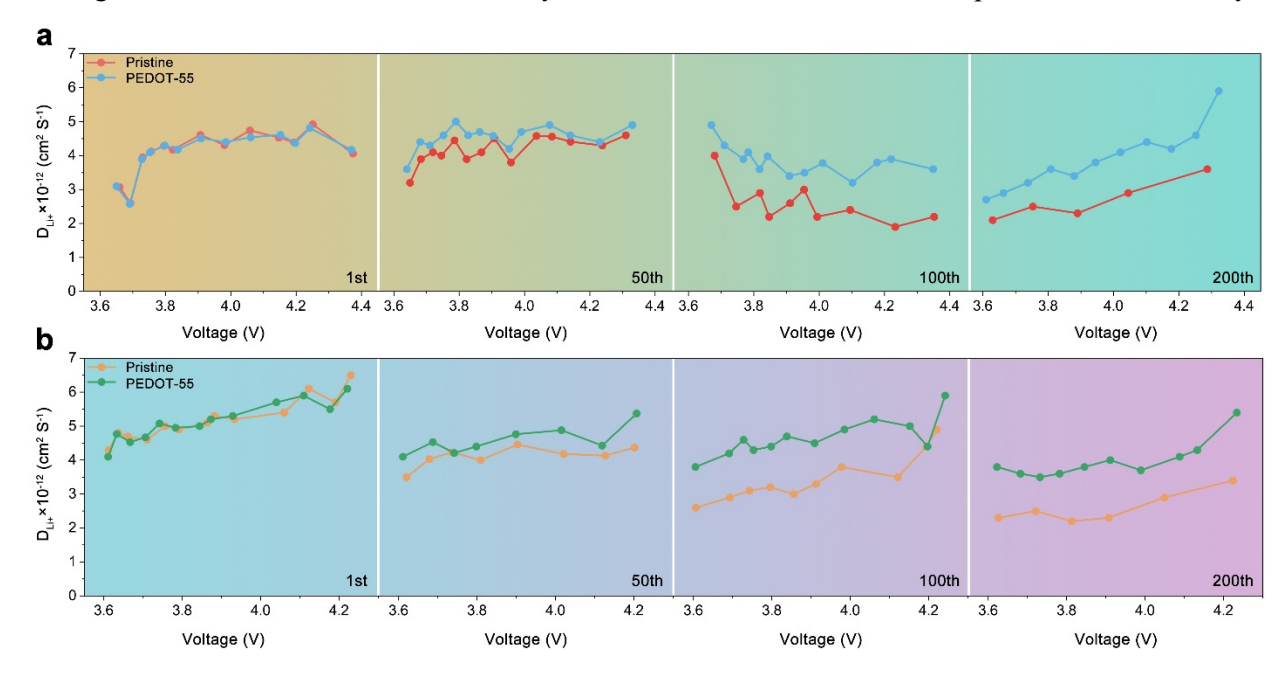


Fig. 4 Excellent lithium transmission ability with circulation. (**A** and **B**) Diffusion coefficients from the GITT potential profiles for pristine and PEDOT-55 samples as a function of the state of charge (A) and discharge (B) at 1st, 50th, 100th and 200th cycle.

Interfacial, structural, and thermal stability

To elucidate the effect of oCVD PEDOT enfolding on the CEI elemental configuration at the nanoscale, TOF-SIMS was employed since the method is known as a highly surface-sensitive analytic technique with a typical chemical selectivity (down to parts-per-billion) and mass resolution (m/ δ m > 7000) to all chemical components in the sample [50]. Pristine NCM811 and PEDOT-55 that were cycled 200 times in coin-type half cells were compared through TOF-SIMS investigations. The integrated intensity obtained from the CEI species of pristine NCM811 and PEDOT-55 is summarized in Fig. 5a, b where major ions of PO₂-, NiF₃- and C₂HO- are detected from both samples with minor ions of POF₂-, CoF₃- and CHO₂-. The TOF-SIMS

profiles as a function of sputtering time, from which the integrated intensity was calculated, were also provided in Fig. S12a-c. It is clearly shown in Fig. 5a and 5b that the intensity of ions (CHO₂⁻, C₂HO⁻, POF₂⁻, PO₂⁻, etc.) in the pristine NCM811 is more than three times as high as that of the PEDOT-55, which indicates the electrolyte in the pristine NCM811 sample has been significantly decomposed, compared to the modified PEDOT-55. The total amount of the dissolved transition metal (TM) species [51] (NiF₃⁻, CoF₃⁻, etc.) in pristine NCM811 is much larger than that of PEDOT-55 as well. The electrolyte decomposition due to aggravated electrode/electrolyte interactions shown in the pristine NCM811 may form a larger amount of CEI with many unfavorable species accumulated on the NCM811 surface, which limits the transportation of lithium ions.

To visualize the distribution and quantify the thickness of CEI, 3D depth profiles obtained from the CEI of the pristine NCM811 and PEDOT-55 were analyzed as a function of TOF-SIMS sputtering time. Three dominating species C₂HO⁻, PO₂⁻ and NiF₃⁻ (as shown in Fig. 5a and 5b) were chosen to represent the decomposition of electrolyte and the dissolution of transition metal elements in the cathode materials. The sulfur-related ion of SO₃⁻ shown in Fig. 5d was selected to represent the PEDOT coating since SO₃⁻ is originated from the sulfur in PEDOT.

For the pristine sample after 320 s (corresponding to \sim 8 nm etched from the initial surface), the intensity of PO₂⁻ and C₂HO⁻ 3D images is basically unchanged compared to the initial surface (i.e., 0 s), which means the CEI caused by decompositions of lithium salt-related compounds (P-containing) and organic solvents (C-containing) strongly prevails at this position of the pristine cathode. Until 640 s sputter time (\sim 17 nm etched), planar-structured CEI is observed. However, the rest of the high intensity regions in the C₂HO⁻ and PO₂⁻ fragments displays thorn-like distributions till the end of the sputtering time, which notably implies that CEIs formed at the micro-voids and -gaps between the primary particles in the pristine cathode due to parasite reactions. The thorn-like CEIs are marked with white rectangles in Fig. 5c.

In Fig. 5d of PEDOT-55 SIMS profiles, the SO₃⁻ fragments are strongly detected from 320 s (8 nm etched) to the entire end, which illustrates that the coating layer is abundantly dispersed in NCM811 particles. It should be particularly emphasized that the high intensity regions of the four SO₃⁻ 3D images represent the presence of oCVD PEDOT in the micro voids between the primary particles, highlighted by white rectangles in Fig. 5d. The SO₃⁻ SIMS images further confirm that oCVD PEDOT successfully filled the micro-gaps between the primary particles. Note that similar regions (i.e., micro voids) in the pristine sample were filled with CEIs.

It should be noted that the low intensity "cap" initially shown in the SO₃ fragment (i.e., 0 s etch) nearly vanished after 320 s etch. In addition, the SIMS intensity of C₂HO⁻, PO₂, and NiF₃ is also found to be weak after 320 s etching time. According to these SIMS intensities, it is reasonable to conclude that in the oCVD PEDOT-modified cathode, the majority of CEI is present as a planar structure until the sputtering time of 320 s. The reaction barrier capability of the conformality coated oCVD PEDOT should be emphasized, by which the formation of CEIs is critically restricted after ~320 s, particularly thorn-like CEIs shown in the pristine cathode.

In addition, the overall structure of the CEI in both cathodes (pristine and PEDOT-coated) consists of a double-layer structure (as indicated by the grey bar in Fig. S13a and S13b): the inorganic species (PO₂⁻, POF₂⁻, NiF₃⁻, CoF₃⁻) are accumulated at the outer sphere while the electrolyte decomposition fragments (C₂HO⁻, CHO₂⁻) are dominating at the inner layer. The detailed analysis was provided in the supplementary

materials.

To estimate the thickness of the CEIs of both samples, ⁶⁰Ni⁻ was selected as the gauge to demonstrate the distribution of the NCM811 particles. In Fig. 5c, ⁶⁰Ni⁻ is detected from 10% sputtering time, which is attributed to the planar-like CEI that predominantly consists of C and P-related species as evidenced in Fig. 5c. The thickness of the planar-like CEI above the cathode is identified to be approximately 17 nm (calculated by the sputtering rate of 0.026 nm s⁻¹). Then followed by the thorn-like CEI distributed in the micro-voids and -gaps between the primary particles as demonstrated in the schematic in Fig. 5e (right). The ⁶⁰Ni⁻ in PEDOT-55 is detected from a 40% sputtering time location (~2,560 s), above which two layers of CEI and PEDOT are present. Below the 40% sputtering time location (after 2,560 s), oCVD PEDOT coexists with ⁶⁰Ni⁻ and particularly the oCVD PEDOT is visible in the micro-voids and -gaps between primary particles. The CEI in PEDOT-55 exists at the range from 0% to 5% sputtering time with a thickness of 8 nm planar-structure exhibited in Fig. 5f (right). Thus, the PEDOT layer on the secondary particle is detected from 5% to 40% sputtering time, from which the thickness of the coated oCVD PEDOT is estimated to be 58 nm, close to ~55 nm measured by an ellipsometer.

In order to identify the resilience performance of oCVD PEDOT coating during battery cycles, microstructures of cycled battery cathodes with pristine and PEDOT-55 were investigated with TEM/HR-TEM and SAED patterns (Fig. S14). Two batteries with pristine and PEDOT-55 were cycled for 100 times under a 1C discharge rate. Fig. S14a shows that the oCVD PEDOT (marked by the yellow line) is well preserved on the surface of the NCM811 particle without any delamination or damages, which leads to superior interfacial reliability for PEDOT-55. An HR-TEM image in Fig. S14b displays minimal rock-salt phases (less than 3 nm in few regions). However, the pristine sample after 100 cycles in Fig. S14c-d shows critical structure evolutions at/near the surface of NCM811 with dominant rock salt phases, evidenced in the HR-TEM (Fig. S14d) and associated SAED patterns (Fig. S14d). The thick rock salt structure formed in the pristine NCM may significantly deteriorate the battery capacity and the ion transport. This comparative TEM analysis confirms that conformal oCVD PEDOT is decidedly effective in restricting the unfavorable phase transformation of the cathode NCM 811 by eliminating adverse side reactions.

The cathode of both PEDOT-55 and pristine NCM 811 battery samples were further examined by SEM after 200 cycles. The dissembled cathode was rinsed with dimethyl carbonate to remove the residual electrolyte. The SEM images in Fig. S15 reveal that pristine NCM811 has several cracks on the surface after circulation, of which the cracks are clearly observed with marked arrows. The formation of microcracks is related to structural rearrangements at a high state of charge (SOC) [26]. The transformation from H2 to H3 phase at potentials above 4.0 V is accompanied by large anisotropic volume changes causing microcracks at the phase boundaries between the crystallites of the secondary particles. Furthermore, a broken structure secondary particle is shown which is dropped out from its main body (marked with a white circle). The exposed surface would drastically decompose the electrolyte and form NiO impurity phases. On the contrary, particles in PEDOT-55 maintain a well-structured shape without any microcracks visible. This comparison suggests that the detrimental phase transformation from H2 to H3 at high SOC is promisingly prohibited by the oCVD PEDOT layer. Due to the absence of cracks, the electrolyte does not make contact with the highly reactive Ni⁴⁺ that may generate a thick CEI layer, which corresponds to the TOF-SIMS results shown in Fig. 5.

To identify the thermal stability and safety of the cathode at high SOC, which is of fundamental relevance

to general battery applications, differential scanning calorimetry (DSC) analysis was adopted. Fig. S16 shows the DSC curves of pristine NCM811 and PEDOT-55 charged at 4.3 V. The pristine NCM811 electrode exhibits an exothermic peak at 233 °C with an enthalpy change (\triangle H) of 713 J g⁻¹. For PEDOT-55, the exothermic peak is located at 246 °C and the enthalpy is 607 J g⁻¹. The higher exothermic peak and lower enthalpy of the PEDOT-55 sample confirm the phase transformation of NCM811 from layered rhombohedral structures to disordered spinel or rock salt structures has been successfully restrained. Hence, the PEDOT layer has been verified to enhance the thermal stability of NCM811.

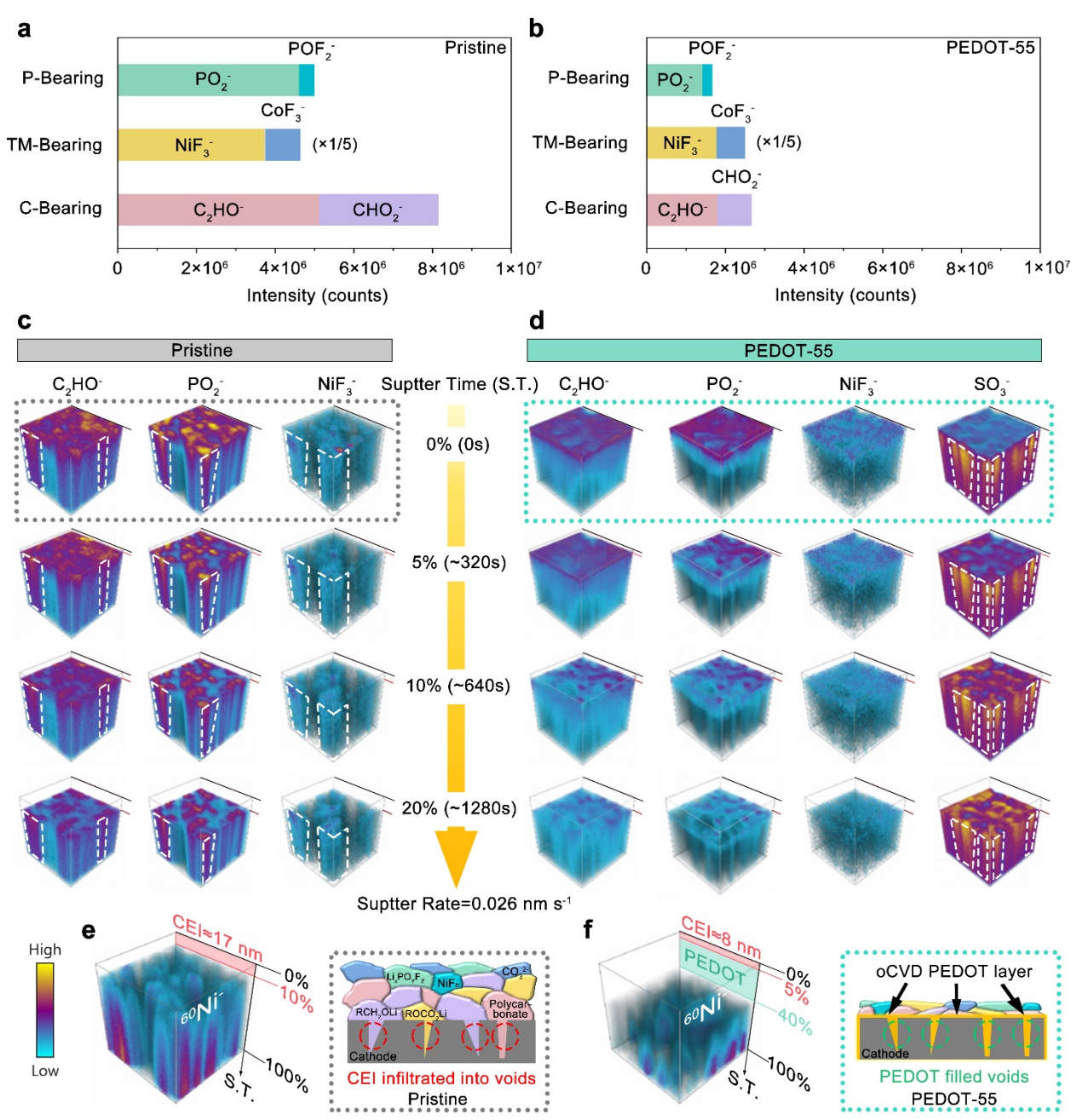


Fig. 5 ToF-SIMS characterization for different samples. Integrated intensities of the secondary-ion fragments detected from the pristine NCM811 (a) and PEDOT-55 (b) respectively. 3D depth profiles of

major secondary-ion fragments constituting the CEI of pristine NCM811 (c) and PEDOT-55 (d) as a function of sputter time. (e) 3D visualization of quantized CEI thickness (left) and schematic of the CEI of pristine NCM811 (right). (f) 3D visualization of the quantized thickness of CEI and PEDOT coating layer (left) and schematic of the CEI of PEDOT-55 (right).

Remote effects on lithium metal anode (LMA)

The production of high-performance lithium metal batteries has shown to be vital to achieving high energy density [52]. To evaluate the effects of oCVD PEDOT to prevent transition metal dissolution on the LMA performance, batteries with pristine and modified cathodes were disassembled after 50 cycles and 150 cycles, and the characteristics of the two LMAs were compared. In Fig. 6a-d, SEM micrographs compare the LMA morphology of the batteries (50 cycles and 150 cycles). SEM images (Fig. 6a) obtained from the LMA paired with the pristine (LMA:Pristine) sample display sponge-like porous structures after 50 cycles showing critically different morphologies to that of the LMA paired with PEDOT-55. The porous structure is likely associated with the mossy lithium and solid-electrolyte interphases (SEIs) [21, 53]. Then, the surface of the LMA is entirely covered by the lithium composites and SEIs after 150 cycles (Fig. 6b). However, an SEM topographic structure demonstrates that the LMA paired with PEDOT-55 (LMA:PEDOT-55) secures the dense morphology with limited microstructure evolutions after cycles of lithium shown in Fig. 6d and 6E after 50 cycles and 150 cycles, respectively, where only minor granules are observed after 150 cycles (Fig. 6e). EDS elemental maps (from Fig. 6b and 6e) are shown in Fig. 6c and 6f. The EDS maps clearly relate that the LMA of the pristine sample contains more C and O on the surface which corresponds to the surface reaction products or substantial SEIs on the surface, compared to that of PEDOT-55, showcasing significantly reduced contaminant and/or reaction products. In addition, the stronger Ni signals are detected on the anode surface of the pristine battery as well, which further evidences an inferior performance due to more rigorous Ni dissolution, migration, and deposition on the anode of the pristine battery.

Stark differences between the two LMAs (i.e., paired with pristine and PEDOT-55 cathodes) are also observed in the electrochemical performance as well. The LMAs were further assembled into Li-Li symmetric batteries with fresh lithium metal to investigate the electrochemical performance. The LMA paired with pristine cathode shows many unstable funnel-shaped fluctuations of the voltage at 1 mA cm⁻² in Fig. 6g. On the contrary, the LMA paired with PEDOT-55 demonstrates a lower over-potential and much-enhanced stability. The restricted transition metal dissolution by PEDOT coating provides an extra benefit on the electrochemical performance of LMA, which improves the cycling stability of the battery as illustrated in Fig. 6h.

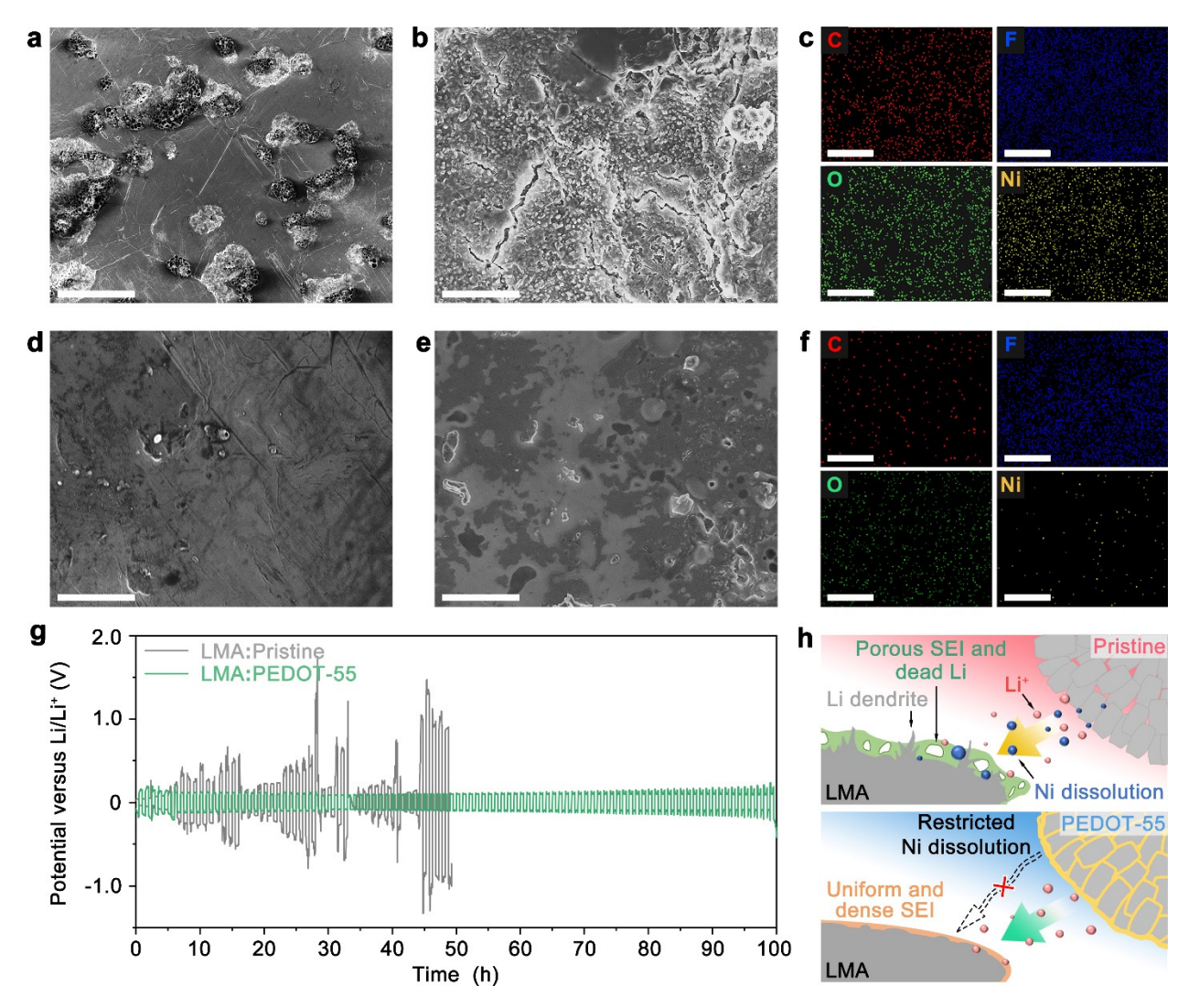


Fig. 6 Morphology and electrochemical characterization of cycled LMA. SEM images of LMA paired with pristine cathode sample after 50 (**a**) and 150 cycles (**b**) under a 1C charge and discharge rate. (**c**) EDS mapping of (b). SEM images of LMA paired with PEDOT-55 cathode sample after 50 (**d**) and 150 cycles (**e**) under a 1C charge and discharge rate. (**f**) EDS mapping of (e). Scale bars, 10 μm (a to f). (**g**) Electrochemical performance for Li-Li symmetric batteries at a current density of 1.0 mA cm⁻² with a cycling capacity of 2.0 mAh cm⁻² (corresponding to 2 h for each step). (**h**). Schematic of remote effect on LMA.

Conclusion

To summarize, we have demonstrated a multi-functional cathode coating strategy by exploiting unique features of oCVD PEDOT, particularly for the Ni-rich cathode of NCM811 in lithium-ion batteries. Gas phase species in the oCVD process are conformally infiltrated into the gaps between the primary particles and coated on the surface of secondary particles. A series of characterizations revealed that the oCVD PEDOT was chemisorbed on the surface of cathode particles with sturdy S-O bonds at the interface. The obtained PEDOT layer equipped with high electronic conductivity generated the conductive networks with

CNTs that significantly reduced the amount of inactive additives while enhancing electronic conductivity and hence noticeably reducing the contact resistance at the interface between the electrolyte and cathode. In addition, the adhesive ability of the oCVD polymer realized the minimal use of traditional polymer binders and consequently further increased the energy density of the batteries. Furthermore, the flexible nature of the polymer provides the enhanced resiliency of the cathode, which enabled the accommodation of the volume changes during circulation. The optimized cathode exhibited about 80% capacity retention after 300 cycles at 1C. Ionic conductivity variation in pristine NCM811 samples and PEDOT-55 were detected by GITT during circulation, which demonstrated that the PEDOT layer well protected the surface from high charge transfer resistance. TOF-SIMS investigations confirmed the oCVD PEDOT coated NCM811 critically limited the formation of undesirable CEIs. The demonstrated cathode design strategy may be of important relevance to not only Ni-rich cathode design studies but also other battery electrode designs since the suggested approach is applicable to LiFePO₄ and Li-rich as a generic design strategy.

Experimental section

Cathode preparing

Electrodes with a high active material weight ratio were prepared in a thin film mixture that consists of NCM811 particles (Sigma Aldrich), Carbon nanotubes (CNTs) as a weight ratio of 99:1 coated onto Al foil. CNTs were uniformly dispersed into N-Methyl-2-pyrrolidone (NMP) in the CNT/NMP weight ratio of 1:30. The as-fabricated electrodes were dried at 120 °C. Then deposited with PEDOT layer and cut into 12 mm in diameter. A custom-designed oCVD system was employed to conformally coat a PEDOT film on the cathode material. 3,4-Ethylenedioxythiophene (EDOT, 97%, Sigma Aldrich) monomers were vaporized at 130 °C and introduced to the sealed vacuum chamber, of which the flow rate was controlled by a needle valve. Iron chloride (FeCl₃ Sigma Aldrich) was used as the oxidant and was sublimated at 165 °C from a crucible in the reactor. During the oCVD PEDOT process, the overall working pressure with the conditions was consistently maintained at 2x10⁻³ Torr. For the battery cathode application, the cathode of LiNi_{0.8}Co_{0.1}Mn_{0.1}O₂ particles (Sigma Aldrich) on Al was attached to the substrate stage and the substrate temperature was kept at 100 °C. To ensure the high uniformity of the resulting PEDOT films, the substrate was rotated at a rate of 5 rpm during deposition. After the oCVD process, the samples were rinsed with methanol to remove residual oxidants and un-reacted monomers and then followed by drying in a vacuum oven at 80 °C.

Electrochemical measurements

Coin cells (CR2032) were assembled and sealed in an argon-filled glove box with 1 M LiPF₆ dissolved in ethylene carbonate, dimethyl carbonate, and diethyl carbonate (EC/DMC/DEC) (1:1:1 in volume rate) as the electrolyte, metallic lithium, and Celgard 2400 membrane as anode and separator, respectively. Galvanostatic discharge/charge tests were conducted in a Land CT2001A battery test system (Jinnuo Wuhan Corp., China) at current densities ranging from 0.1C to 7C (1C=200 mA g⁻¹) at ambient temperature (~25 °C). The cyclic voltammetry (CV) curves were measured using an electrochemical workstation (VersaSTAT3 Princeton) at the scan rate of 0.1 mV s⁻¹, and electrochemical impedance spectroscopy (EIS) measurements were performed under a frequency range of 100 kHz–0.01 Hz using a vibration voltage of 5.0 mV. Li-Li symmetric cells were assembled in the glovebox with lithium metal anodes paired with pristine and modified cathodes respectively. The cycled lithium metal anode was rinsed with dimethyl

carbonate (DMC) to remove the residual lithium salt. Galvanostatic cycling was performed for Li-Li symmetric cells at a current density of 1.0 mA cm⁻² with a cycling capacity of 2.0 mAh cm⁻² (corresponding to 2 h for each step).

Chemo-physical analysis

The thickness of the PEDOT on the Si substrate was measured by an FS-1 Ellipsometer (Film Sense). The chemical and physical properties of the samples were determined by Fourier-transform infrared spectroscopy (FTIR, Nexus 670 ThermoNicolet Spectrometer). The particle surface elemental and valence states were examined by X-ray photoelectron spectroscopy (Thermo Fisher Scientific NEXSA). Time-offlight secondary ion mass spectrometry (TOF-SIMS) analysis, in particular depth profiling, was conducted with a TOF-SIMS instrument (IONTOF GmbH) with a 30 keV Bi1 analysis ion beam and a 250 eV Cs sputtering ion beam for negative secondary-ion fragments enhanced detection. All prepared samples were transferred to the TOF-SIMS instrument via an in-house designed air-free setup. During depth profiling in either polarity, the typical acquisition area was 100 µm × 100 µm and centered within the Cs 300 µm x 300 μ m sputtered area. The Cs sputtering rate for the cathode was ≈ 0.026 nm s⁻¹. Integrated yields of secondaryion fragments of interest were obtained by integrating the full-width-half-maximum area of the secondary ion yield curves in the depth profiles. The differential scanning calorimetry method (DSC/DTA-TG, STA 449 F3 Jupiter) was implanted at a constant heating rate of 10 °C min⁻¹ from ambient condition to 400 °C. For ex-situ TOF-SIMS and DSC tests, the electrodes were disassembled from the coin cells in the required state of charge, then the electrode material was washed by anhydrous DMC and sealed in a penicillin bottle. The disassembling procedures above were carried out in an argon-filled glovebox.

Morphology characterization

A scanning electron microscopy (SEM) system (FEI Nova NanoSEM) was used to investigate the morphology of the samples. In addition, transmission electron microscopy (TEM) and high-resolution transmission electron microscopy (HRTEM) images were acquired in a microscope (FEI Themis Z) to examine the morphologies and structural details of the samples. A Helios G4 UC (Thermofisher Scientific) focused ion beam (FIB)/SEM dual-beam system was deployed to prepare a TEM specimen from a PEDOT coated cathode particle through a standard lift-out procedure. To reveal the spatial distribution of the PEDOT coating layer, the TEM and energy-dispersive X-ray spectrometer were used for HAADF imaging and elemental mapping.

DFT Simulation

DFT calculations were performed using the Vienna ab initio simulation package (VASP). These calculations utilized the Perdew–Burke–Ernzerhof (PBE) GGA exchange-correlation functional, and the projector augmented wave (PAW) method. D2 dispersion was utilized to account for Vander Waals interactions. The adsorption of EDOT to a 3-layer thick LiNiO₂ surface with 10 Å of vacuum space. An energy cut-off of 800 eV was used to give well-converged energies for the LiNiO₂ surface with and without adsorbates present. All structures were fully optimized using the default VASP convergence criteria.

Acknowledgments

Competing Interests

The authors declare that they have no competing interests.

Data and materials availability

All data needed to evaluate the conclusions in the paper are present in the paper and/or the Supplementary Materials.

References

- [1] M. Armand, J.M. Tarascon, Building better batteries, Nature 451(7179) (2008) 652-657.
- [2] J.M. Tarascon, M. Armand, Issues and challenges facing rechargeable lithium batteries, Nature 414(6861) (2001) 359-367.
- [3] Y.-K. Sun, S.-T. Myung, B.-C. Park, J. Prakash, I. Belharouak, K. Amine, High-energy cathode material for long-life and safe lithium batteries, Nature Materials 8(4) (2009) 320-324.
- [4] J.B. Goodenough, K.S. Park, The Li-ion rechargeable battery: a perspective, J Am Chem Soc 135(4) (2013) 1167-76.
- [5] M.S. Whittingham, Lithium Batteries and Cathode Materials, Chemical Reviews 104(10) (2004) 4271-4302.
- [6] J.B. Goodenough, Cathode materials: A personal perspective, Journal of Power Sources 174(2) (2007) 996-1000.
- [7] H.-x. Wei, Y.-d. Huang, L.-b. Tang, C. Yan, Z.-j. He, J. Mao, K. Dai, X.-w. Wu, J.-b. Jiang, J.-c. Zheng, Lithium-rich manganese-based cathode materials with highly stable lattice and surface enabled by perovskite-type phase-compatible layer, Nano Energy 88 (2021) 106288.
- [8] J. Kim, H. Lee, H. Cha, M. Yoon, M. Park, J. Cho, Prospect and Reality of Ni-Rich Cathode for Commercialization, Advanced Energy Materials 8(6) (2018) 1702028.
- [9] P. Rozier, J.M. Tarascon, Review—Li-Rich Layered Oxide Cathodes for Next-Generation Li-Ion Batteries: Chances and Challenges, Journal of The Electrochemical Society 162(14) (2015) A2490-A2499.
- [10] H. Zheng, R. Yang, G. Liu, X. Song, V.S. Battaglia, Cooperation between Active Material, Polymeric Binder and Conductive Carbon Additive in Lithium Ion Battery Cathode, The Journal of Physical Chemistry C 116(7) (2012) 4875-4882.
- [11] A. Manthiram, A reflection on lithium-ion battery cathode chemistry, Nature Communications 11(1) (2020) 1550.
- [12] P. Guan, L. Zhou, Z. Yu, Y. Sun, Y. Liu, F. Wu, Y. Jiang, D. Chu, Recent progress of surface coating on cathode materials for high-performance lithium-ion batteries, Journal of Energy Chemistry 43 (2020) 220-235.
- [13] Q. Xie, W. Li, A. Manthiram, A Mg-Doped High-Nickel Layered Oxide Cathode Enabling Safer, High-Energy-Density Li-Ion Batteries, Chemistry of Materials 31(3) (2019) 938-946.
- [14] Y.-C. Li, W. Xiang, Z.-G. Wu, C.-L. Xu, Y.-D. Xu, Y. Xiao, Z.-G. Yang, C.-J. Wu, G.-P. Lv, X.-D. Guo, Construction of homogeneously Al3+ doped Ni rich Ni-Co-Mn cathode with high stable cycling performance and storage stability via scalable continuous precipitation, Electrochimica Acta 291 (2018) 84-94.
- [15] D. Kong, J. Hu, Z. Chen, K. Song, C. Li, M. Weng, M. Li, R. Wang, T. Liu, J. Liu, M. Zhang, Y. Xiao, F. Pan, Ti-Gradient Doping to Stabilize Layered Surface Structure for High Performance High-Ni Oxide Cathode of Li-Ion Battery, Advanced Energy Materials 9(41) (2019) 1901756.
- [16] K. Min, S.W. Seo, Y.Y. Song, H.S. Lee, E. Cho, A first-principles study of the preventive effects of Al and Mg doping on the degradation in LiNi0.8Co0.1Mn0.1O2 cathode materials, Phys Chem Chem Phys 19(3) (2017) 1762-1769.
- [17] X. Luo, X. Wang, L. Liao, S. Gamboa, P.J. Sebastian, Synthesis and characterization of high tap-density layered Li[Ni1/3Co1/3Mn1/3]O2 cathode material via hydroxide co-precipitation, Journal of Power Sources 158(1) (2006) 654-658.
- [18] W. Hua, J. Zhang, Z. Zheng, W. Liu, X. Peng, X.D. Guo, B. Zhong, Y.J. Wang, X. Wang, Na-doped Ni-rich LiNi0.5Co0.2Mn0.3O2 cathode material with both high rate capability and high tap density for lithium ion batteries, Dalton Trans 43(39) (2014) 14824-32.
- [19] Q. Li, R. Dang, M. Chen, Y. Lee, Z. Hu, X. Xiao, Synthesis Method for Long Cycle Life Lithium-Ion Cathode

- Material: Nickel-Rich Core-Shell LiNi0.8Co0.1Mn0.1O2, ACS Applied Materials & Interfaces 10(21) (2018) 17850-17860.
- [20] Y. Cho, S. Lee, Y. Lee, T. Hong, J. Cho, Spinel-Layered Core-Shell Cathode Materials for Li-Ion Batteries, Advanced Energy Materials 1(5) (2011) 821-828.
- [21] M. Yoon, Y. Dong, J. Hwang, J. Sung, H. Cha, K. Ahn, Y. Huang, S.J. Kang, J. Li, J. Cho, Reactive boride infusion stabilizes Ni-rich cathodes for lithium-ion batteries, Nature Energy 6(4) (2021) 362-371.
- [22] F. Wu, S. Fang, M. Kuenzel, A. Mullaliu, J.-K. Kim, X. Gao, T. Diemant, G.-T. Kim, S. Passerini, Dual-anion ionic liquid electrolyte enables stable Ni-rich cathodes in lithium-metal batteries, Joule (2021).
- [23] Y. Kim, H. Park, K. Shin, G. Henkelman, J.H. Warner, A. Manthiram, Rational Design of Coating Ions via Advantageous Surface Reconstruction in High-Nickel Layered Oxide Cathodes for Lithium-Ion Batteries, Advanced Energy Materials 11(38) (2021) 2101112.
- [24] L.-b. Tang, Y. Liu, H.-x. Wei, C. Yan, Z.-j. He, Y.-j. Li, J.-c. Zheng, Boosting cell performance of LiNi0.8Co0.1Mn0.1O2 cathode material via structure design, Journal of Energy Chemistry 55 (2021) 114-123.
- [25] X.-M. Fan, Y.-D. Huang, H.-X. Wei, L.-B. Tang, Z.-J. He, C. Yan, J. Mao, K.-H. Dai, J.-C. Zheng, Surface Modification Engineering Enabling 4.6 V Single-Crystalline Ni-Rich Cathode with Superior Long-Term Cyclability, Advanced Functional Materials 32(6) (2022) 2109421.
- [26] G.-L. Xu, Q. Liu, K.K.S. Lau, Y. Liu, X. Liu, H. Gao, X. Zhou, M. Zhuang, Y. Ren, J. Li, M. Shao, M. Ouyang, F. Pan, Z. Chen, K. Amine, G. Chen, Building ultraconformal protective layers on both secondary and primary particles of layered lithium transition metal oxide cathodes, Nature Energy (2019).
- [27] K. Du, H. Xie, G. Hu, Z. Peng, Y. Cao, F. Yu, Enhancing the Thermal and Upper Voltage Performance of Ni-Rich Cathode Material by a Homogeneous and Facile Coating Method: Spray-Drying Coating with Nano-Al2O3, ACS Applied Materials & Interfaces 8(27) (2016) 17713-17720.
- [28] F. Schipper, H. Bouzaglo, M. Dixit, E.M. Erickson, T. Weigel, M. Talianker, J. Grinblat, L. Burstein, M. Schmidt, J. Lampert, C. Erk, B. Markovsky, D.T. Major, D. Aurbach, From Surface ZrO2 Coating to Bulk Zr Doping by High Temperature Annealing of Nickel-Rich Lithiated Oxides and Their Enhanced Electrochemical Performance in Lithium Ion Batteries, Advanced Energy Materials 8(4) (2018) 1701682.
- [29] X. Xiong, Z. Wang, G. Yan, H. Guo, X. Li, Role of V2O5 coating on LiNiO2-based materials for lithium ion battery, Journal of Power Sources 245 (2014) 183-193.
- [30] G.-R. Hu, X.-R. Deng, Z.-D. Peng, K. Du, Comparison of AlPO4- and Co3(PO4)2-coated LiNi0.8Co0.2O2 cathode materials for Li-ion battery, Electrochimica Acta 53(5) (2008) 2567-2573.
- [31] K. Min, K. Park, S.Y. Park, S.-W. Seo, B. Choi, E. Cho, Improved electrochemical properties of LiNi0.91Co0.06Mn0.03O2 cathode material via Li-reactive coating with metal phosphates, Scientific Reports 7(1) (2017) 7151.
- [32] J. Zheng, M. Gu, J. Xiao, B.J. Polzin, P. Yan, X. Chen, C. Wang, J.-G. Zhang, Functioning Mechanism of AlF3 Coating on the Li- and Mn-Rich Cathode Materials, Chemistry of Materials 26(22) (2014) 6320-6327.
- [33] P. Yan, J. Zheng, M. Gu, J. Xiao, J.-G. Zhang, C.-M. Wang, Intragranular cracking as a critical barrier for high-voltage usage of layer-structured cathode for lithium-ion batteries, Nature Communications 8(1) (2017) 14101.
- [34] Y.-N. Zhou, J.-L. Yue, E. Hu, H. Li, L. Gu, K.-W. Nam, S.-M. Bak, X. Yu, J. Liu, J. Bai, E. Dooryhee, Z.-W. Fu, X.-Q. Yang, High-Rate Charging Induced Intermediate Phases and Structural Changes of Layer-Structured Cathode for Lithium-Ion Batteries, Advanced Energy Materials 6(21) (2016) 1600597.
- [35] G. Liu, H. Zheng, S. Kim, Y. Deng, A.M. Minor, X. Song, V.S. Battaglia, Effects of Various Conductive Additive

- and Polymeric Binder Contents on the Performance of a Lithium-Ion Composite Cathode, Journal of The Electrochemical Society 155(12) (2008).
- [36] M.E. Spahr, D. Goers, A. Leone, S. Stallone, E. Grivei, Development of carbon conductive additives for advanced lithium ion batteries, Journal of Power Sources 196(7) (2011) 3404-3413.
- [37] B. Han, Y. Yang, X. Shi, G. Zhang, L. Gong, D. Xu, H. Zeng, C. Wang, M. Gu, Y. Deng, Spontaneous repairing liquid metal/Si nanocomposite as a smart conductive-additive-free anode for lithium-ion battery, Nano Energy 50 (2018) 359-366.
- [38] S.G.I. John P. Lock, Karen K. Gleason, Oxidative Chemical Vapor Deposition of Electrically Conducting Poly(3,4-ethylenedioxythiophene) Films, Macromolecules 39(16) (2006) 4.
- [39] S.G. Im, E.A. Olivetti, K.K. Gleason, Systematic control of the electrical conductivity of poly (3,4-ethylenedioxythiophene) via oxidative chemical vapor deposition (oCVD), Surface and Coatings Technology 201(22-23) (2007) 9406-9412.
- [40] C. Yuan, B. Gao, L. Su, L. Chen, X. Zhang, Electrochemically Induced Phase Transformation and Charge-Storage Mechanism of Amorphous CoS[sub x] Nanoparticles Prepared by Interface-Hydrothermal Method, Journal of The Electrochemical Society 156(3) (2009).
- [41] T.-H. Wu, Y.-C. Lin, B.-W. Hou, W.-Y. Liang, Nanostructured β–NiS Catalyst for Enhanced and Stable Electro–oxidation of Urea, Catalysts 10(11) (2020).
- [42] Y.-C. Lu, A.N. Mansour, N. Yabuuchi, Y. Shao-Horn, Probing the Origin of Enhanced Stability of "AlPO4" Nanoparticle Coated LiCoO2 during Cycling to High Voltages: Combined XRD and XPS Studies, Chemistry of Materials 21(19) (2009) 4408-4424.
- [43] R. Jung, R. Morasch, P. Karayaylali, K. Phillips, F. Maglia, C. Stinner, Y. Shao-Horn, H.A. Gasteiger, Effect of Ambient Storage on the Degradation of Ni-Rich Positive Electrode Materials (NMC811) for Li-Ion Batteries, Journal of The Electrochemical Society 165(2) (2018) A132-A141.
- [44] H.S. Liu, Z.R. Zhang, Z.L. Gong, Y. Yang, Origin of Deterioration for LiNiO[sub 2] Cathode Material during Storage in Air, Electrochemical and Solid-State Letters 7(7) (2004).
- [45] J.P. Lock, J.L. Lutkenhaus, N.S. Zacharia, S.G. Im, P.T. Hammond, K.K. Gleason, Electrochemical investigation of PEDOT films deposited via CVD for electrochromic applications, Synthetic Metals 157(22-23) (2007) 894-898.
- [46] H. Chelawat, S. Vaddiraju, K. Gleason, Conformal, Conducting Poly(3,4-ethylenedioxythiophene) Thin Films Deposited Using Bromine as the Oxidant in a Completely Dry Oxidative Chemical Vapor Deposition Process, Chemistry of Materials 22(9) (2010) 2864-2868.
- [47] J. Sicklinger, M. Metzger, H. Beyer, D. Pritzl, H.A. Gasteiger, Ambient Storage Derived Surface Contamination of NCM811 and NCM111: Performance Implications and Mitigation Strategies, Journal of The Electrochemical Society 166(12) (2019) A2322-A2335.
- [48] R.A.H. W. Weppner, Determination of the Kinetic Parameters of Mixed-Conducting Electrodes and Application to the System Li3Sb, Journal of The Electrochemical Society 124(10) (1977) 9.
- [49] P.P. Prosini, M. Lisi, D. Zane, M. Pasquali, Determination of the chemical diffusion coefficient of lithium in LiFePO4, Solid State Ionics 148(1) (2002) 45-51.
- [50] A. Benninghoven, Chemical Analysis of Inorganic and Organic Surfaces and Thin Films by Static Time-of-Flight Secondary Ion Mass Spectrometry (TOF-SIMS), Angewandte Chemie International Edition in English 33(10) (1994) 1023-1043.
- [51] J. Li, W. Li, Y. You, A. Manthiram, Extending the Service Life of High-Ni Layered Oxides by Tuning the

Electrode-Electrolyte Interphase, Advanced Energy Materials 8(29) (2018) 1801957.

[52] W. Xu, J. Wang, F. Ding, X. Chen, E. Nasybulin, Y. Zhang, J.-G. Zhang, Lithium metal anodes for rechargeable batteries, Energy & Environmental Science 7(2) (2014) 513-537.

[53] C. Fang, X. Wang, Y.S. Meng, Key Issues Hindering a Practical Lithium-Metal Anode, Trends in Chemistry 1(2) (2019) 152-158.